



PAPER

## 3D printing on glass for direct sensor integration

To cite this article: M Neubauer *et al* 2019 *Eng. Res. Express* 1 025051

View the [article online](#) for updates and enhancements.

### You may also like

- [Principles of Plasma Spectroscopy](#)  
A.L. Osterheld
- [Sixth International Colloquium on Atomic Spectra and Oscillator Strengths \(ASOS 6\)](#)  
Wolfgang L Wiese and Donald C Morton
- [All Polymeric Electrochemical Biochip Array of Patterned Gold on Silver Inkjet Printed Polyimide](#)  
Richa Pandey, Matteo Beggiato, Yelena Sverdlov et al.



## PAPER

## 3D printing on glass for direct sensor integration

RECEIVED  
1 October 2019REVISED  
25 November 2019ACCEPTED FOR PUBLICATION  
4 December 2019PUBLISHED  
13 December 2019

M Neubauer, M McGlennen, S Thomas and S Warnat

Mechanical and Industrial Engineering &amp; Center for Biofilm Engineering Montana State University, United States of America

E-mail: [stephan.warnat@montana.edu](mailto:stephan.warnat@montana.edu)

Keywords: 3d printing, glass substrate, sensor packaging, additive manufacturing

**Abstract**

Significant improvements are being made in 3D printed microfluidics. 3D printing of microfluidic prototypes gained importance due to the fabrication flexibility compared to conventional techniques. Applications using these devices often require optical access to internal channels but even clear resins create translucent channels due to surface roughness and imperfections. This paper describes a 3D printing approach to form fluidic channels directly onto glass substrates that allows optical access to fluidic channels without distortion from 3D printing material. The glass substrate is itself a part of the flow channel which allows optical transparency. Micro-fabricated conductivity and impedance spectroscopy sensors were fabricated on glass substrates and placed in a custom made 3D printer build plate before fluidic structures are directly printed on top of the sensors. The effects on sensor performance and properties were evaluated using co-linear four-point probe resistance measurements, Raman spectroscopy, and impedance spectroscopy. It was shown that no resin or other chemicals are left behind from the printing procedure and sensor performance was unaffected. A proof of concept impedance-conductivity sensor was integrated with a 3D printed flow channel and shown to work as both conductivity and bacterial cells detection sensor.

**1. Introduction**

Additive manufacturing (AM) is becoming an increasingly viable option for the creation of fluidic devices [1–6]. Vat polymerization printing (VPP) such as stereolithography (SLA) and digital light processing (DLP) are popular techniques for creating 3D printed microfluidics due to their high resolution [7, 8]. The resolution of various printing techniques such as VPP, material extrusion, and material jetting are compared in [1–3, 5, 7]. 3D printing allows one-step creation of fluidic devices with high throughput and straightforward device parameter adjustment in Computer-Aided Design (CAD) software. Designs and devices can be distributed and replicated in different facilities by merely sharing the design files [1]. Commercial availability of printers and resins capable of truly microfluidic (sub 100  $\mu\text{m}$  features) devices is somewhat limited [9]. In this paper, we demonstrate the integration of micro-fabricated sensors on glass with a high-resolution 3D printing technique.

Optically transparent surfaces within microfluidic devices are essential for accurate quantification of chemical, biological, and mechanical interactions [10]. Many 3D printing resins, however, are not clear, and while the use of clear resins theoretically allow for the creation of transparent devices, inherent surface imperfections can cause light diffusion creating translucent channels. There are several examples in the literature of devices printed on glass to create a very smooth surface using SLA and DLP techniques. Urrios *et al* utilized a glass build plate and glass vat to decrease surface roughness and increase print transparency in bio-microfluidic devices [11]. Gong *et al* constructed a custom printer to create microfluidic devices on glass substrates in order to avoid using an anodized aluminum build plate and to provide optical access to internal microfluidic components [12–14]. Parker *et al* 3D printed microfluidic devices with immunoaffinity monoliths on glass allowing for fluorescence measurements for the extraction of preterm birth biomarkers [15]. Lee *et al* 3D printed Quake style valves using glass as a build plate to increase channel visibility, eliminating the need to remove the device from the build plate, and to provide a flat, stable surface for a microscope stage [16]. Kim *et al* printed multiple designed microchannels on glass for convenient optical access [17, 18]. Beauchamp *et al* characterized

the 3D printing of sub-100  $\mu\text{m}$  external and internal, positive and negative resolution features and additionally created a particle trapping device with the particles clearly seen as viewed through glass [19]. Beauchamp *et al* again printed on glass to create visible microfluidic channels and fluorescent emission of preterm birth biomarkers inside the channel was collected [20]. Rogers *et al* fabricated 3D printed microfluidic channels with valves, and claimed that their ability to print directly on glass opened the possibility for direct integration of printing on materials with patterned electrodes [21]. The previous examples of printing on glass utilized base layers to ensure proper attachment, limiting the possibility of direct interaction between sensor material and fluids. Rather than printing directly on glass, Plevniak *et al* used an SLA printer to print a 50  $\mu\text{m}$  open channel and then covalently bonded to glass post-printing resulting in a closed hollow channel [22]. Notably, Kou *et al* printed microfluidic channels directly on glass without the use of base layers to create an optical window for phase-contrast microscopy and fluorescence microscopy. [23]. However, a direct sensor integration in the 3D printed fluidic channel was not shown.

Integrating sensors for 3D printed fluidics is reviewed by Li *et al* [24]. Banna *et al* embedded pH and conductivity sensors into a fused deposition modeling (FDM) 3D print post-print allowing for sensor removal and replacement [25]. Using a print-pause-print technique, Gaal *et al* demonstrated a process for directly integrating an FDM printed structure with an electronic sensor by printing directly on the sensor rather than inserting the sensor post-print. Gold interdigitated electrodes (IDEs) were evaporated on a transparency sheet and a polydimethylsiloxane (PLA) channel was printed directly onto the transparency sheet creating an integrated electronic tongue sensor with optical window for increased channel visibility [26]. Pol *et al* described a fully integrated screen-printed sulfide-selective sensor on a 3D printing potentiometric microfluidic platform accomplished by a screen-printing step between two main FDM printing stages [27]. Di Nova *et al* designed, fabricated and tested a fully aerosol jet printed (AJP) electrochemical microfluidic sensor. Dispensed and cured silver-silver chloride and carbon ink formed electrochemical sensing elements on an alumina substrate while UV-curable polymer ink created a flow channel surrounding the sensing elements [28]. While these techniques work well for sensor integration, none utilize a glass substrate for optically clear channels.

Glass substrates are a viable method for creating optically transparent channels using high resolution printing techniques such as VPP or material jetting described above, however sensor integration often requires a multi-step integration process. In this paper, a glass based impedance-conductivity sensor is directly integrated with a 3D printed flow channel as a proof of concept device. This device is shown to work as both a conductivity sensor and bacterial cells detector. This is accomplished by printing directly on a glass substrate with patterned electrodes without the use of base layers using a DLP resin printer. Build plate modification and glass silane treatment facilitated this direct integration. The motivation for optical access in flow channels is well documented above and further explored below. Resin-printer deficiencies were overcome and sensor performance and properties were quantified both before and after device printing. Finally, sensor functionality is demonstrated with various conductivity and bacterial cells solutions. This work is significant because the advancement and advantages of 3D printed microfluidics described above can be directly integrated with sensors to study biological processes.

## 2. Methods

### 2.1. Printer integration

A MiiCraft 50 was the 3D printer utilized in this work. This printer uses 405 nm light to selectively cure polymer to form 3D structures by area-projecting light using DLP as described in [7]. Clear BV007 resin (MiiCraft) was chosen for its advertised low viscosity, transparency, and printer compatibility.

A build plate was manufactured with a 20  $\times$  25 mm insert, shown in figure 1. Using a silicone gasket and a diaphragm vacuum pump (Masis, GZ35-12) a glass slide could be held in place during the printing process and quickly released afterwards. The glass slide protruded slightly from the plane of the build plate; this distance was measured and accounted for in the printer software. Mounting the glass flush with the edge of the insert made it possible to reference the edge of the glass in the software so that prints could be precisely aligned to the edges of the glass itself with better than 100  $\mu\text{m}$  repeatability.

Diced borosilicate glass (BSG) substrates (Borofloat 33, University Wafer), 20 mm  $\times$  25 mm  $\times$  700  $\mu\text{m}$ , were submerged in a 2.0 vol% solution of 3-(trimethoxysilyl) propyl methacrylate in ethanol (Bind-Silane, GE Healthcare, 17-1330-01) for five minutes, then submerged in ethanol for five minutes, and finally held at 105  $^{\circ}\text{C}$  for five minutes. This silane treatment protocol has been used to couple polymerizing hydrogel to a glass surface [29], but also worked to couple the resin used in this work to the glass without using an initial base layer.

Upon printing completion, the print was submerged in a solution of Resin Away (Monocure PTY LTD) and sonicated for 1 min, or until all uncured resin was removed. The print and substrate were rinsed with deionized

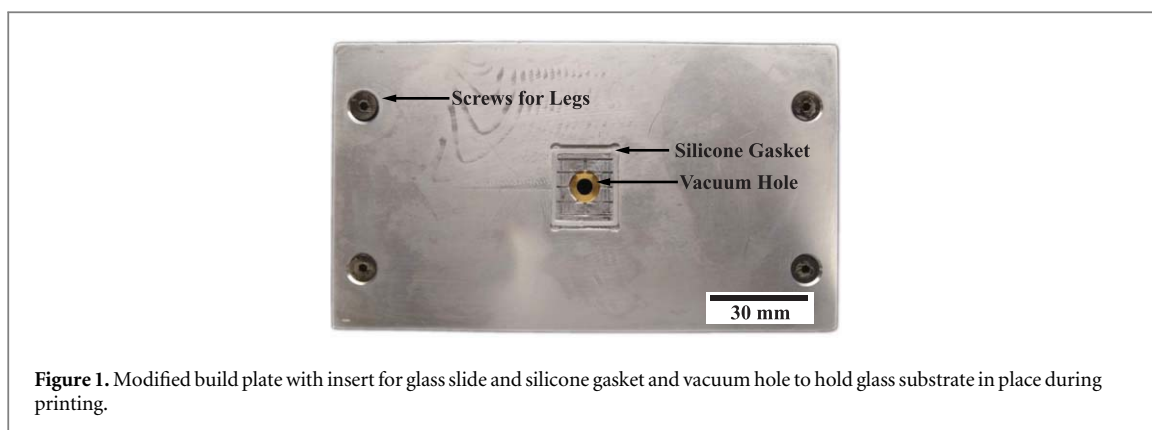


**Figure 1.** Modified build plate with insert for glass slide and silicone gasket and vacuum hole to hold glass substrate in place during printing.

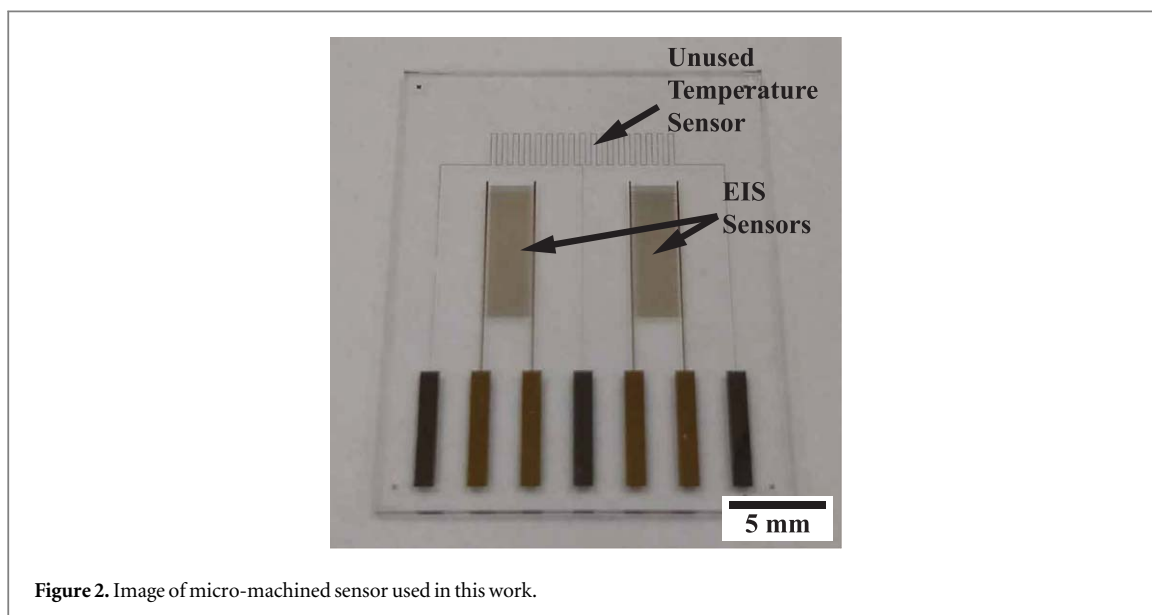


**Figure 2.** Image of micro-machined sensor used in this work.

water and post-cured in B9 Model Cure (B9Creations, USA) for 20 s. Lab grade isopropanol was found to be less effective than Resin Away, as it would often cause the print to crack.

Physical vapor deposition (PVD) with thermal evaporation was used to deposit 10 nm of Cr adhesion layer, followed by electron-beam evaporation to deposit a 100 nm layer of Au onto a 700  $\mu\text{m}$  thick, 100 mm BSG wafer. A positive photolithography process and wet chemical etch defined the patterned sensor, seen in figure 2. The wafer was diced into nine 20  $\times$  25 mm sensors. These sensors were designed originally as temperature and electrochemical impedance spectroscopy (EIS) sensors, however in this work the temperature function was not utilized.

A flow chart outlining the fabrication process is shown in figure 3(a). Due to the limitation of the resin used in this work, printing closed channels was not deemed feasible. Instead, channels were printed open and a second print was used as a cover. The open channel and cover were each printed on glass and alignment features were designed on the open channel. A #3 round brush was used to lightly coat the contact surface of the open channel with uncured resin and then the cover was aligned and held firmly in place with a clamp during a post-cure process which fused the two prints together, resulting in a well-defined closed channel seen in figure 3(b). While using two prints to create closed channels was possible and repeatable, using a resin capable of closed channels would still be preferred in order to create a higher precision, single-step device.

Replaceable 3D printed barb style adapters allowed tubing (1 mm ID, 3 mm OD, Tygon R-3603) to be connected to the flow channel for fluid introduction. Double-sided Kapton tape was used as an intermediate layer between the channel inlet/outlet and the barb adapter. While this was enough to secure the adapter for a short period of time, magnets (R422-N52, K&J Magnets) were used to secure the adapters for longer intervals with higher bursting pressure. These replaceable adapters seen in figures 3(b) and (c) resembled those used by Atencia *et al* but rather than a blunt needle, a barb connector was printed [30]. One of the advantages of printing adapters is that it can be assured that the liquid from the tube never interacts with the surface of the magnet.

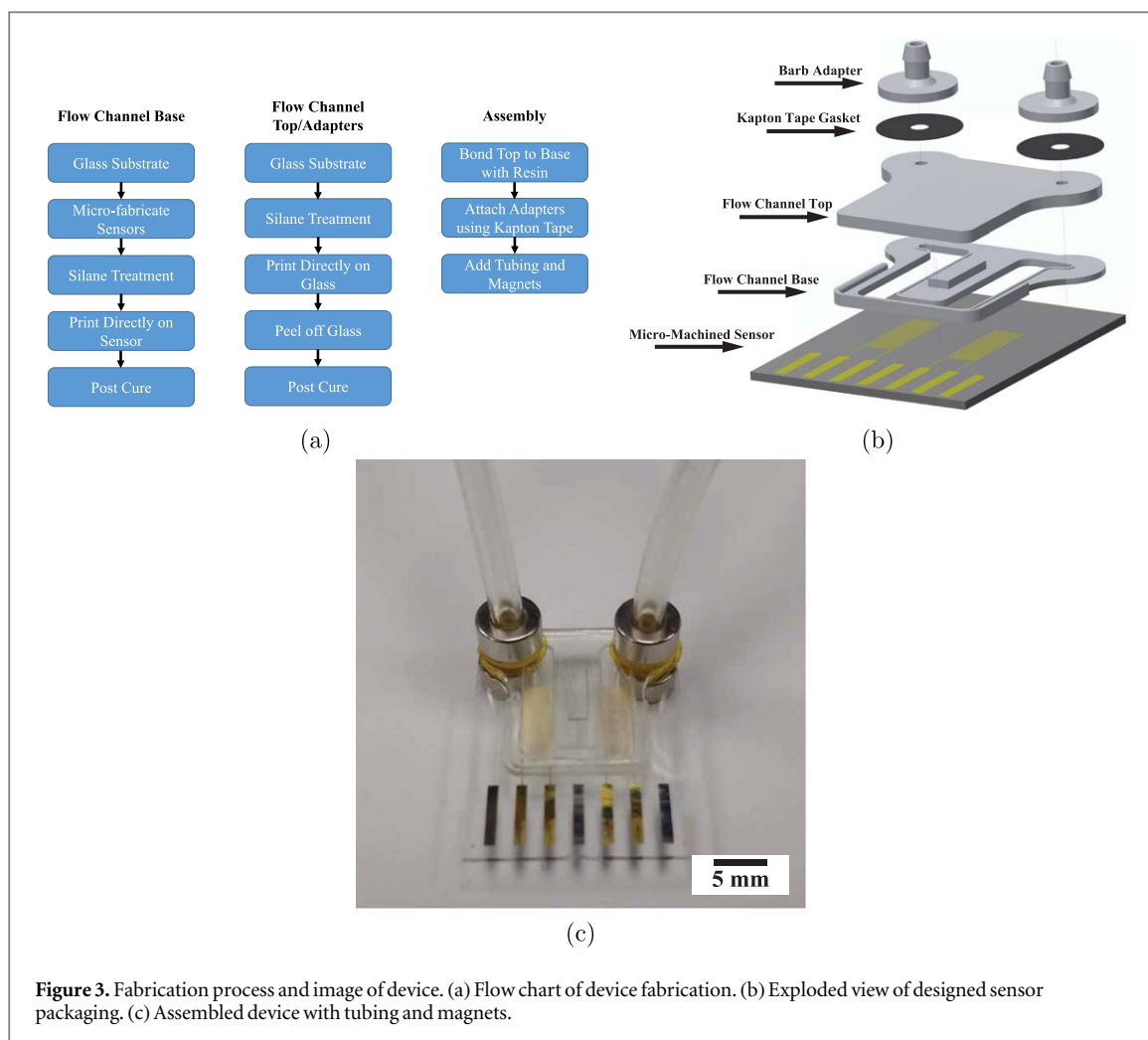


**Figure 3.** Fabrication process and image of device. (a) Flow chart of device fabrication. (b) Exploded view of designed sensor packaging. (c) Assembled device with tubing and magnets.

The adapters were printed on glass without the use of base layers so that the sealing face of the adapters was smooth and consistent print to print. A 1 mm hollow punch was used to create a consistently sized hole in the tape and then the adapter was centered and pressed onto the tape. A 7 mm hollow punch was used to cut out the tape in a circle slightly larger than the adapter. When ready for use the protective sheet was removed from the backside of the tape and pressed onto the flow channel inlet/outlet. The tubing was attached to the barb adapter and a ring magnet fit around the tubing onto the adapter. A second, disc magnet (D42-N52, K&J Magnets) provided the clamping magnetic force from the backside of the substrate.

## 2.2. Component characterization

Light transmission through sample printed on glass was measured with a spectrophotometer (FastSpec 528, MicroLab, USA) to quantify optical clarity of printing on glass. The transmittance, defined as the ratio of light which passed through the sample to the incident light, was recorded in this manner. 502 nm and 660 nm light was emitted from an LED towards a light detector and the intensity was measured. Measurements were taken by placing a 3D printed sample between the LED and detector. One sample of each thickness was measured 5–10 times at these two wavelengths.

To demonstrate the improved image clarity provided by printing directly on a glass substrate, 275  $\mu\text{m}$  microbeads (REDPMS-1.080 250–300  $\mu\text{m}$ , Cospheric, USA) were placed in a suspension solution and directed through the integrated flow channel on the sensor under a microscope. Images were collected viewing the microbeads through both the glass substrate and through the printed flow channel.

The bursting pressure of the magnetic adapters was tested in a similar manner to [30]. A printed solid cylinder and adapter were attached with a piece of Kapton tape. The printed cylinder simulated the flow channel to which adapters were attached. For consistency, cylinders were printed on glass and peeled off and post-cured with the glass side being the side to which the tape was affixed. Tubing connected the adapter to a 10 ml Becton Dickson syringe placed in a Kent Scientific GenieTouch syringe pump. The adapter end of the tubing was submerged in water so that the appearance of bubbles marked the point at which the connection began to leak. The volume of air in the tubing and syringe was noted. Approximating air as an ideal gas, the ideal gas law could

be rearranged into equation (1)

$$P = P_a V_i / (V_i - dV) \quad (1)$$

where  $P_a$  is atmospheric pressure,  $V_i$  is the initial volume recorded, and  $dV$  is the volume dispensed by the syringe pump, respectively. The guaranteed pressure applied by the syringe pump for this specific syringe according to the manufacturer was approximately 6 atm. Atencia *et al* found a bursting pressure of approximately 5 atm using a similar procedure with Kapton tape and magnets [30].

### 2.3. Device characterization

Resistance measurements were performed on Au samples with identical deposition parameters in order to quantify the effect of the silane treatment on sensor performance. A custom-built co-linear four-point probe with 1.3 mm needle tip spacing and a Keithley 2450 SMU were used to conduct the measurements. Spherical spring-loaded testing tips with a diameter of 0.6 mm were used to guarantee a good electrical contact (uxcell P11J). Ten consecutive readings of each current polarity were acquired and averaged. This was repeated ten times for two samples before and after silane treatment.

In order to confirm no resin or other chemicals are left behind from the printing process or silane treatment, three sensors from the same process wafer were investigated with Raman spectroscopy. One sensor was left untreated, a second received the silane treatment, and the third received the silane treatment and the base of the flow channel was printed on the sensor. A spectra was collected from a spot both on the glass and the gold from each sensor with a Horiba Labram HR Evolution Raman spectrometer. Additionally, a scan of the cured resin was captured.

The impedance spectra of a conductivity standard (Biopharm 84  $\mu\text{S cm}^{-1}$ ) collected before and after printing, with and without magnets was obtained in order to confirm the sensor performance remained unchanged due to printing. Before applying the silane treatment and packaging the sensor, a flow channel with the same dimensions (not printed on glass) was printed and clamped on top of the sensor using a silicone gasket to seal the channel. Three spectra were obtained using a Hioki IM3536 LCR in the range of 1 kHz–8 MHz, rinsing the flow channel with deionized water between measurements. Another three spectra were obtained with the magnets for the barb adapters in place. Three more spectra with and without magnets were obtained after printing was complete.

### 2.4. Sample applications

As a proof of concept application, various conductivity solutions were synthesized using conductivity standards (Biopharm) and deionized milli-Q water (GenPure xCAD Plus, Thermo Scientific, 18.2 M $\Omega\text{cm}$ ). Solutions of 21, 42, 63, 84, 141 and 353  $\mu\text{S cm}^{-1}$  were created using milli-Q water to dilute 84 and 1413  $\mu\text{S cm}^{-1}$  conductivity standards with the assumption that the milli-Q water had an insignificant conductivity relative to the conductivity standards. Impedance spectra from 1 kHz–8 MHz were collected in the same manner as described previously. A frequency of 100 kHz was chosen to calculate the conductivity. Using a linear model for the conductivity-temperature relationship shown in equation (2), a temperature coefficient  $\alpha$  was calculated using equation (3)

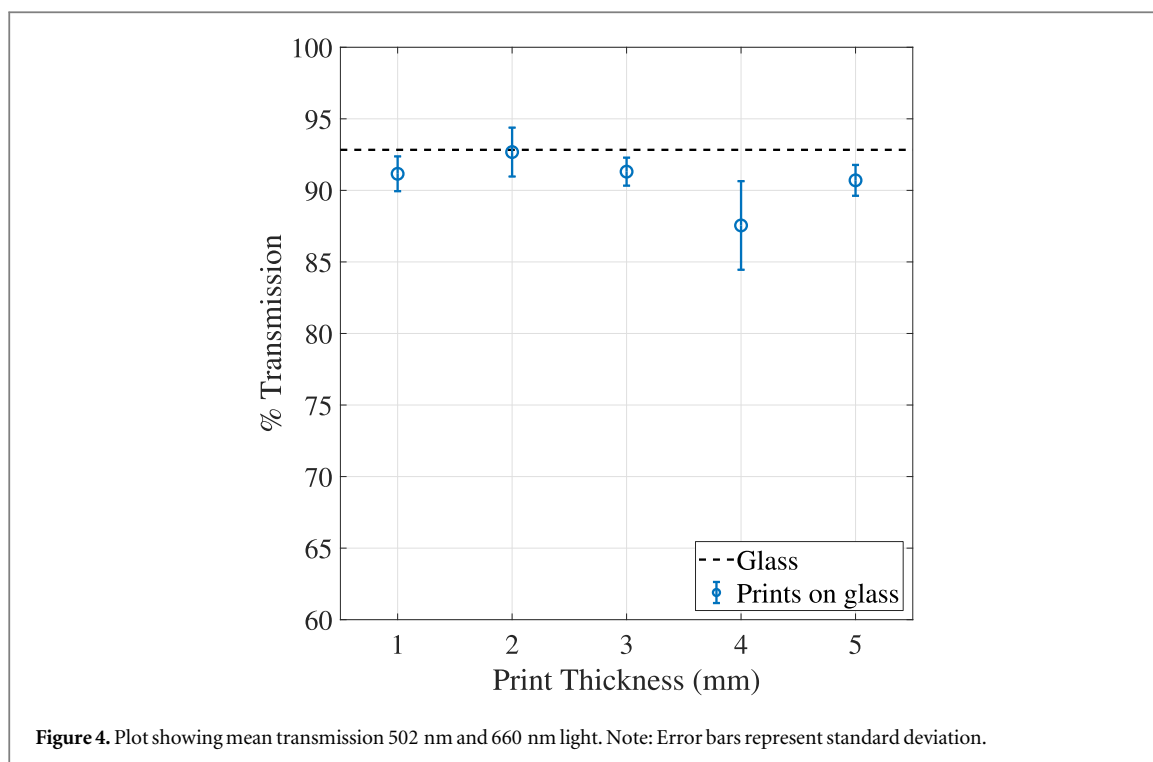
$$\kappa = \kappa_{ref} (1 + \alpha(T - T_{ref})) \mu\text{S cm}^{-1} \quad (2)$$

$$\alpha = \frac{\kappa - \kappa_{ref}}{\kappa_{ref} (T - T_{ref})} * 100 \% \text{ } ^\circ\text{C}^{-1} \quad (3)$$

where  $\kappa$  and  $T$  were the measured conductance and temperature and  $\kappa_{ref}$  and  $T_{ref}$  were the advertised conductivity at the reference temperature of 25  $^\circ\text{C}$ , respectively.

As another proof of concept application, *Escherichia coli* K12 cells were suspended in milli-Q water and different dilutions were analyzed using impedance spectroscopy. A Petri dish was removed from refrigerator stock, and a single colony of *E. coli* K12 was scraped from a Petri dish, and introduced into a 50 ml Falcon tube containing 25 ml of 1X tryptic soy broth (TSB; BD Bacto). The Falcon tube was inserted into an incubator (37  $^\circ\text{C}$ ) with orbital shaker (150 RPM) for 19 h. Subsequently, the Falcon tube was centrifuged at 4700 RPM for 10 min. TSB media was replaced from the Falcon tube with 25 ml of autoclaved milli-Q water and thoroughly mixed. Nine 1.5 ml micro-centrifuge tubes were arranged in linear sequence for dilution series. 1 ml of media containing *E. coli* K12 was pipetted from undiluted Falcon tube into a first micro-centrifuge tube, and was thoroughly mixed. Next, 100  $\mu\text{l}$  of media was pipetted from first mixture, and combined with 900  $\mu\text{l}$  of milli-Q water into second micro-centrifuge tube creating a 1:10<sup>1</sup> dilution of *E. coli* K12 cells to milli-Q water. This procedure was repeated until a dilution of 1:10<sup>8</sup> (ninth micro-centrifuge tube) from the original was reached. All steps were performed inside a biosafety cabinet to ensure sterile conditions.

To obtain cell counts, 100  $\mu\text{l}$  of the final four dilution mixtures were pipetted onto Petri dishes containing tryptic soy agar (TSA; BD Bacto) and spread using glass spreaders. The Petri dishes were sealed with parafilm and



left for 24 h at room temperature to incubate. Cell concentrations were performed by counting the individual colony-forming units (CFU) established on each plate, multiplying by the level of dilution, and dividing by the amount of media pipetted.

Yang *et al* performed a similar experiment where *Salmonella* cells were suspended both water and phosphate-buffered saline (PBS) and the impedance response over a range of frequencies were recorded using interdigitated microelectrodes. It was found that cell concentrations could be distinguished down to  $10^6$  CFU/ml and higher in water, while cells suspended in PBS could not be distinguished [31].

### 3. Results and discussion

#### 3.1. Component characterization

The transmittance of a blank glass slide yielded a value within 1% of the theoretical transmission of approximately 92% [32]. Parts printed directly onto glass resulted in transmission values less than that of glass, as seen in figure 4, but still averaged higher than 90%. These data suggest that the 3D prints are not significantly scattering or absorbing the incident light, as the average transmittance is still within 5% to that of glass.

The packaged sensor can be seen in figure 3(b) and again in figure 5(a) with the barb adapters and yellow Kapton tape with magnets and tubing attached. Figure 5(b) shows how the relative position of the microbeads to each finger of the impedance sensor and channel wall is well-defined. In addition, the bead diameter is more easily determined which may be of interest with objects of unknown size. Note: the diameter of the used beads has an advertised variation of  $50 \mu\text{m}$  and our measurements with a calibrated optical microscope were within this tolerance. In contrast, in figure 5(c) the relative microbead position and diameters are more challenging to determine.

During testing of the magnetic connectors, the syringe pump compressed the syringe past the advertised guaranteed force of the syringe pump with one or two exceptions. It's possible the syringe pump is capable of applying more force than advertised, or approximating air as an ideal gas breaks down below 6 atm. In any case, the syringe pump was unable to cause the magnetic adapters to leak by nearly fully compressing 10 ml of air. This was deemed more than adequate for this work.

#### 3.2. Device characterization

After performing the resistance measurements on two gold samples before and after silane treatment, a paired t-test with a double tail p-value of 0.048 and 0.740 was found for sample 1 (pre- and post-treatments) and sample 2 respectively, using the set of ten means. A boxplot showing these data is shown in figure 6(a). The p-values suggest the silane treatment has minimal effect on the resistance of Au used for the sensors in this work.

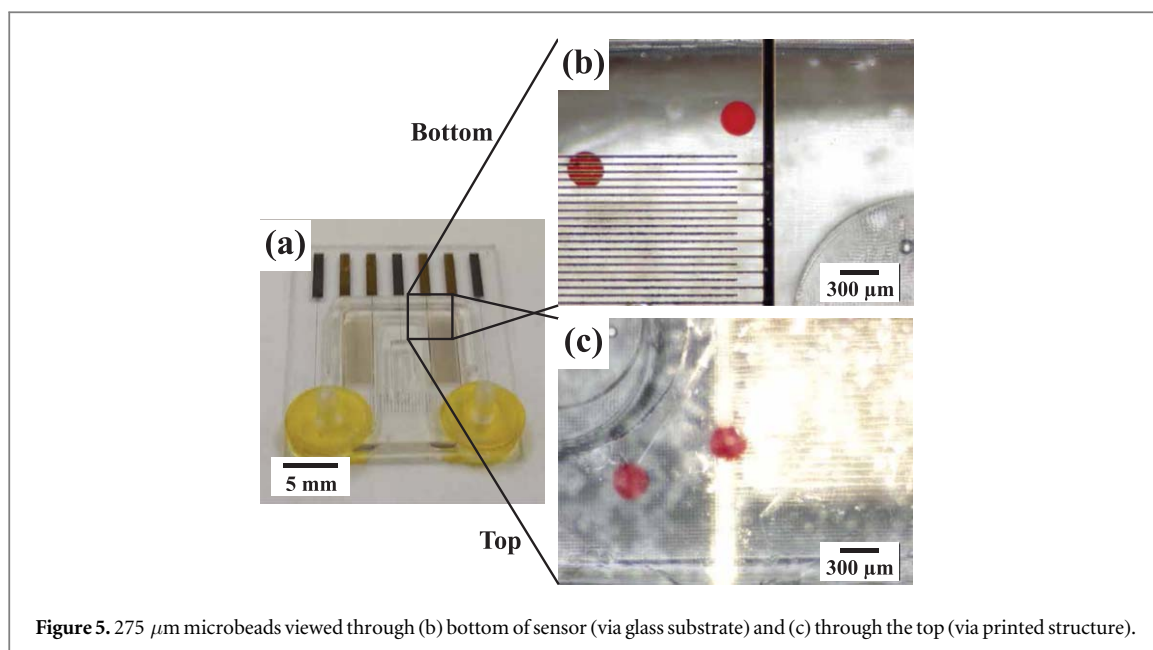


**Figure 5.** 275  $\mu\text{m}$  microbeads viewed through (b) bottom of sensor (via glass substrate) and (c) through the top (via printed structure).

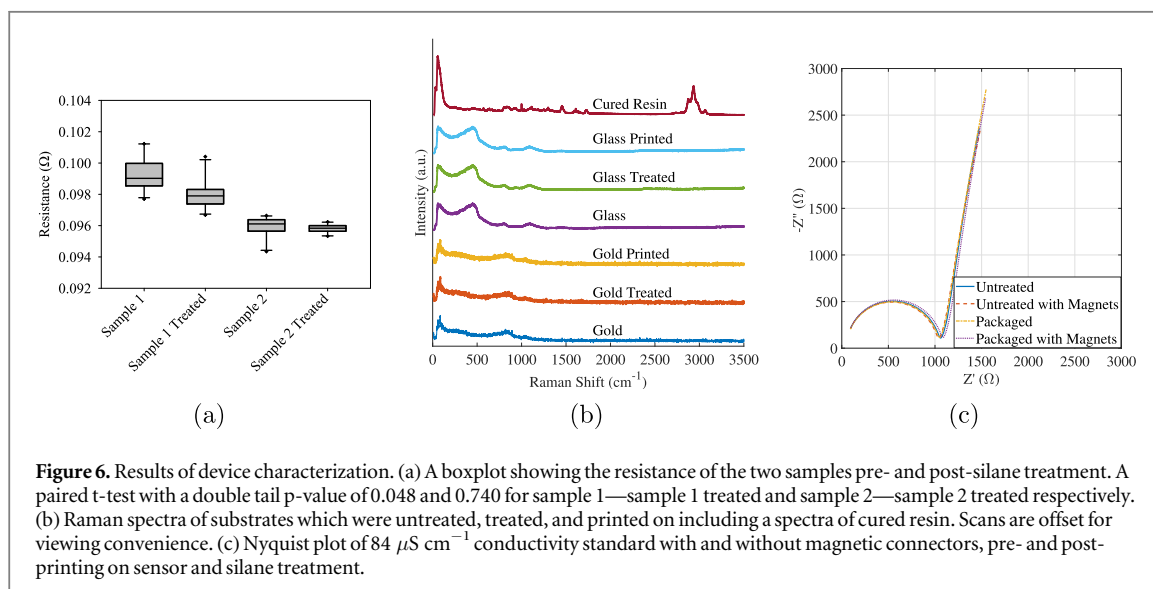


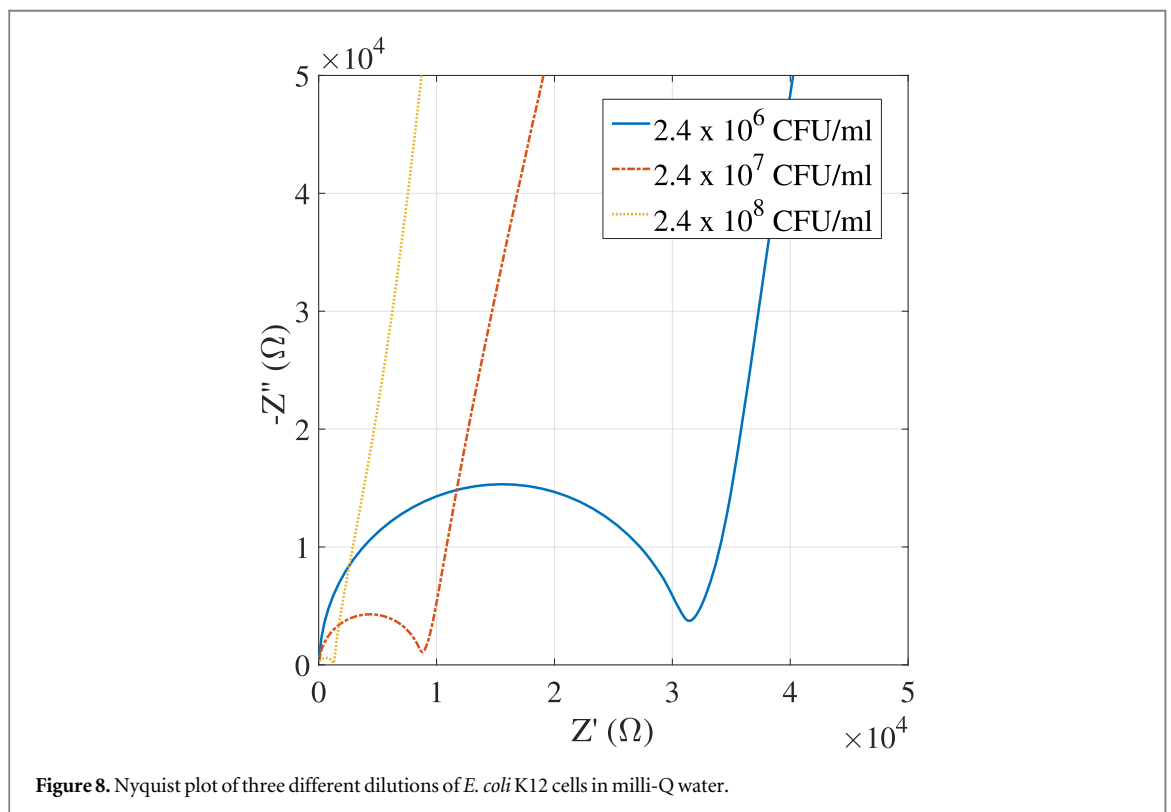
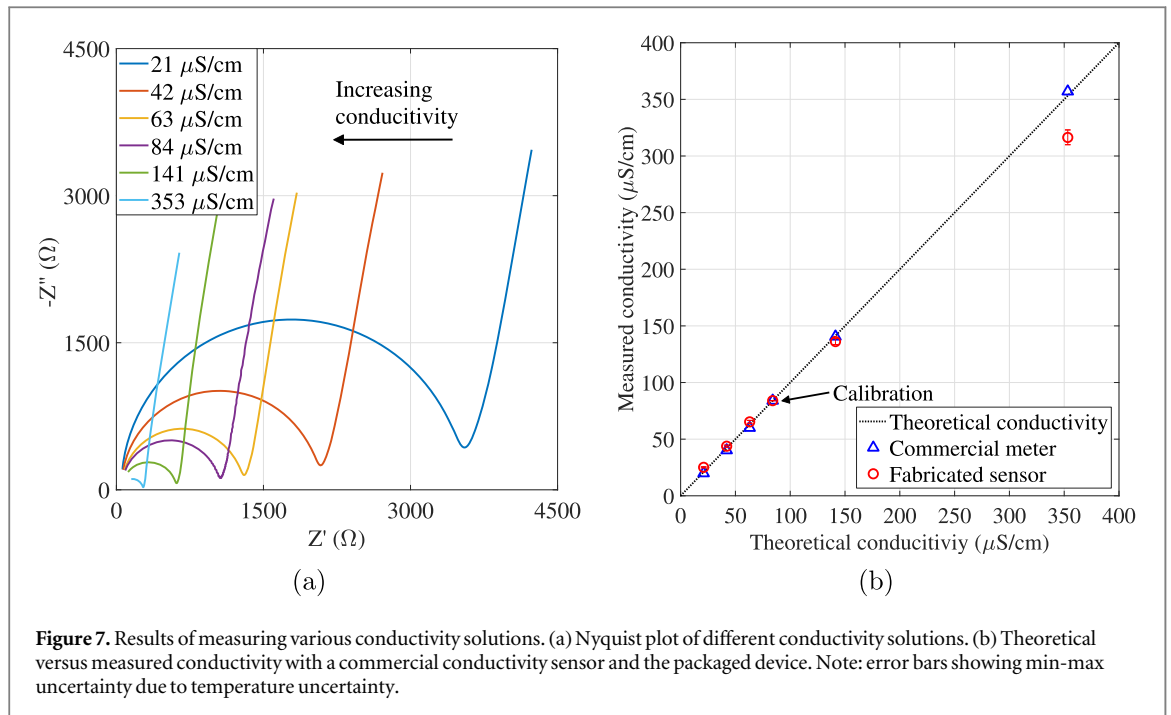
**Figure 6.** Results of device characterization. (a) A boxplot showing the resistance of the two samples pre- and post-silane treatment. A paired t-test with a double tail p-value of 0.048 and 0.740 for sample 1—sample 1 treated and sample 2—sample 2 treated respectively. (b) Raman spectra of substrates which were untreated, treated, and printed on including a spectra of cured resin. Scans are offset for viewing convenience. (c) Nyquist plot of 84  $\mu\text{S cm}^{-1}$  conductivity standard with and without magnetic connectors, pre- and post-printing on sensor and silane treatment.

The Raman spectra are shown in figure 6(b) with the cured resin spectra shown first followed by the glass and gold surfaces pre- and post-silane treatment and post-printing. All gold and glass substrates look alike regardless of silane treatment or printing and none show the peaks of the cured resin around 3000  $\text{cm}^{-1}$ . This suggests that no resin or other chemicals are left on surfaces.

Impedance spectroscopy measurements were performed to evaluate sensor performance before and after the printing on the sensor. These data are plotted in a Nyquist diagram, which shows the real resistance versus the negative imaginary resistance. The curves of the Nyquist plot overlap in figure 6(c) suggesting that sensor performance is negligibly affected by the printing process.

### 3.3. Sample applications

The six conductivity solutions can be clearly distinguished in a Nyquist plot in figure 7(a). The experimental cell constant of 0.083  $2 \text{ cm}^{-1}$  was found by comparing a commercial conductivity meter (Omega, CDS107). Using the linear temperature conductivity model described in equations (2) and (3), the conductivity of the various solutions was calculated and plotted in figure 7(b). The error bars show the min-max uncertainty due to temperature uncertainty. Also plotted is the measured conductivity by the commercial meter. The sensor measured conductivity values within 8% of the meter with the exception of the lowest and highest conductivity



solutions which each varied by more than 12% from the meter. The working range of the sensor is affected by both the cell constant and the linear temperature compensation model.

Impedance spectra were collected from 4 Hz–5 MHz on three dilutions ( $2.4 \times 10^6$ ,  $2.4 \times 10^7$  and  $2.4 \times 10^8$  CFU/ml) of suspended *E. coli* K12 cells and the Nyquist curves are shown in figure 8. The three dilutions are clearly distinguished in this plot and show that this packaged sensor is capable of distinguishing concentrations of bacterial cells down to  $2.4 \times 10^6$  CFU/ml. It was found that lower concentrations of cells could not be distinguished, therefore the detection limit for this sensor is  $2.4 \times 10^6$  CFU/ml for *E. coli* K12 cells suspended in water.

### 3.4. Discussion

The described procedure demonstrates how printing on glass can be applied to an arbitrary micro-machined sensor for integrating 3D printing and sensors. The sample applications were chosen to suit the sensors, however similar micro-fabricated sensors could be designed for many other applications. The procedure of build plate modification and silane treatment are compatible with the higher resolution printers and resins described above, and therefore recent advancements of 3D printed microfluidics can be integrated with micro-fabricated sensors in this described manner.

## 4. Conclusion

In this work, a procedure for direct integration of glass substrate sensing platforms with complex and precise packaging is outlined. The glass substrate is itself a part of the channel and allows ideal optical access. Resistance measurements, Raman spectroscopy, and impedance spectra show that sensor properties are unaffected and no resin or chemicals are left on the sensing surface after printing on the sensor. Viability of materials other than Au could be tested for other applications with similar techniques. Microbeads were imaged through the glass substrate to show the improved optical properties compared to imaging through a thin printed channel wall using clear resin. As proof of concept applications, a simple impedance-conductivity micro-machined sensor was directly integrated with a 3D printed flow channel with a well-defined sensing area and was shown to work as a conductivity sensor and *E. coli* K12 dilution detector with a detection limit of  $2.4 \times 10^6$  CFU/ml. Applying the same methods for device realization, any number of devices can be integrating with a 3D printed structure. The limitations on device design generally are associated with the 3D printer, its resolution and compatible resins. These issues will become less prevalent as the technology in this rapidly advancing field improves and becomes available. Overall, this process will benefit from all advances in 3D printing technologies, becoming an increasingly viable avenue for sensor-packaging integration for bio-sensing.

## Acknowledgments

This work was performed in part at the Montana Nanotechnology Facility, a member of the National Nanotechnology Coordinated Infrastructure (NNCI), which is supported by the National Science Foundation (Grant# ECCS-1542210) and funded by Montana State University (MSU). Transmission measurements were performed with the help of C. Bahn from the MSU Chemistry Department. B Kincaid and G Foster (MSU machine shop) helped manufacture the build plates. We thank the MSU C. Foreman lab for assistance with the *E. coli* K12 preparation.

## ORCID iDs

S Warnat  <https://orcid.org/0000-0001-5032-9320>

## References

- [1] Chen C, Mehl B T, Munshi A S, Townsend A D, Spence D M and Martin R S 2016 3d-printed microfluidic devices: fabrication, advantages and limitations a mini review *Anal. Methods* **8** 6005–12
- [2] Macdonald N P, Cabot J M, Smejkal P, Guijt R M, Paull B and Bredmore M C 2017 Comparing microfluidic performance of three-dimensional (3d) printing platforms *Anal. Chem.* **89** 3858
- [3] Zhou Y 2017 The recent development and applications of fluidic channels by 3d printing *J. Biomed. Sci.* **24** 80–101
- [4] Lepowsky E and Tasoglu S 2018 Emerging anti-fouling methods: towards reusability of 3d-printed devices for biomedical applications *Micromachines* **9** 196
- [5] Mi S, Du Z, Xu Y and Sun W 2018 The crossing and integration between microfluidic technology and 3d printing for organ-on-chips *J. Mater. Chem. B* **6** 6191–206
- [6] Sochol R D, Sweet E, Glick C C, Wu S-Y, Yang C, Restaino M and Lin L 2018 3d printed microfluidics and microelectronics *Microelectron. Eng.* **189** 52–68
- [7] Lee J M, Sing S L, Zhou M and Yeong W Y 2018 3d bioprinting processes: a perspective on classification and terminology *International Journal of Bioprinting* **4** 151–60
- [8] Bhattacharjee N, Urrios A, Kang S and Folch A 2016 The upcoming 3d-printing revolution in microfluidics *Lab Chip* **16** 1720–42
- [9] Gong H, Beauchamp M, Perry S, Woolley A T and Nordin G P 2015 Optical approach to resin formulation for 3d printed microfluidics *RSC Adv.* **5** 106621–32
- [10] Romanov V, Samuel R, Chaharlang M, Jafek A R, Frost A and Gale B K 2018 Fdm 3d printing of high-pressure, heat-resistant, transparent microfluidic devices *Anal. Chem.* **90** 10450–6
- [11] Urrios A et al 2016 3d-printing of transparent bio-microfluidic devices in peg-da *Lab Chip* **16** 2287–94
- [12] Gong H, Woolley A T and Nordin G P 2016 High density 3d printed microfluidic valves, pumps, and multiplexers *Lab Chip* **16** 2450–8
- [13] Gong H, Bickham B P, Woolley A T and Nordin G P 2017 Custom 3d printer and resin for 18  $\mu\text{m}$   $\times$  20  $\mu\text{m}$  microfluidic flow channels *Lab Chip* **17** 2899–909

- [14] Gong H, Woolley A T and Nordin G P 2018 3d printed high density, reversible, chip-to-chip microfluidic interconnects *Lab Chip* **18** 639–47
- [15] Parker E K, Nielsen A V, Beauchamp M J, Almughamsi H M, Nielsen J B, Sonker M, Gong H, Nordin G P and Woolley A T 2019 3d printed microfluidic devices with immunoaffinity monoliths for extraction of preterm birth biomarkers *Anal. Bioanal. Chem.* **411** 5405–13
- [16] Lee Y-S, Bhattacharjee N and Folch A 2018 3d-printed quake-style microvalves and micropumps *Lab Chip* **18** 1207–14
- [17] Kim Y T, Castro K, Bhattacharjee N and Folch A 2018 Digital manufacturing of selective porous barriers in microchannels using multi-material stereolithography *Micromachines* **9** 125
- [18] Kim Y T, Bohjanen S, Bhattacharjee N and Folch A 2019 Partitioning of hydrogels in 3d-printed microchannels *Lab Chip* **19** 3086–93
- [19] Beauchamp M J, Gong H, Woolley A T and Nordin G P 2018 3d printed microfluidic features using dose control in x, y, and z dimensions *Micromachines* **9** 326
- [20] Beauchamp M J, Nielsen A V, Gong H, Nordin G P and Woolley A T 2019 3d printed microfluidic devices for microchip electrophoresis of preterm birth biomarkers *Anal. Chem.* **91** 7418–25
- [21] Rogers C I, Qaderi K, Woolley A T and Nordin G P 2015 3d printed microfluidic devices with integrated valves *Biomicrofluidics* **9** 016501–016501
- [22] Plevniak K, Campbell M, Myers T, Hodges A and He M 2016 3d printed auto-mixing chip enables rapid smartphone diagnosis of anemia *Biomicrofluidics* **10** 054113–054113
- [23] Kuo A P, Bhattacharjee N, Lee Y-S, Castro K, Kim Y T and Folch A 2019 High-precision stereolithography of biomicrofluidic devices *Adv. Mater. Technol.* **4** 1800395
- [24] Li F, Macdonald N P, Guijt R M and Breadmore M C 2019 Increasing the functionalities of 3d printed microchemical devices by single material, multimaterial, and print-pause-print 3d printing *Lab Chip* **19** 35–49
- [25] Banna M, Bera K, Sochol R, Lin L, Najjaran H, Sadiq R and Hoorfar M 2017 3d printing-based integrated water quality sensing system *Sensors (Basel, Switzerland)* **17** 1336
- [26] Gaal G, Mendes M, de Almeida T P, Piazzetta M H O, Gobbi Â L, Riul A and Rodrigues V 2017 Simplified fabrication of integrated microfluidic devices using fused deposition modeling 3d printing *Sensors Actuators B* **242** 35–40
- [27] Pol R, Céspedes F, Gabriel D and Baeza M 2019 Fully integrated screen-printed sulfide-selective sensor on a 3d-printed potentiometric microfluidic platform *Sensors Actuators B* **290** 364–70
- [28] Di Novo N G, Cantù E, Tonello S, Sardini E and Serpelloni M 2019 Support-material-free microfluidics on an electrochemical sensors platform by aerosol jet printing *Sensors (Basel, Switzerland)* **19** 1842
- [29] Benjamin A D, Abbasi R, Owens M, Olsen R J, Walsh D J, LeFevre T B and Wilking J N 2019 Light-based 3d printing of hydrogels with high-resolution channels *Biomed. Phys. Eng. Express* **5** 025035
- [30] Atencia J, Cooksey G A, Jahn A, Zook J M, Vreeland W N and Locascio L E 2010 Magnetic connectors for microfluidic applications *Lab Chip* **10** 246–9
- [31] Yang L 2008 Electrical impedance spectroscopy for detection of bacterial cells in suspensions using interdigitated microelectrodes *Talanta* **74** 1621–9
- [32] Hecht E 2017 *Optics Fifth* (New York: Pearson Education, Inc.) OpticsPearson Education, Incorporated 0133977226